The Journal of Chemical Physics

Pushing the limits: Efficient wavefunction methods for excited states in complex systems using frozen-density embedding

Cite as: J. Chem. Phys. **157**, 204101 (2022); https://doi.org/10.1063/5.0100393
Submitted: 24 May 2022 • Accepted: 31 October 2022 • Accepted Manuscript Online: 01 November 2022 • Published Online: 22 November 2022

Robert S. Treß, Jing Liu, Christof Hättig, et al.

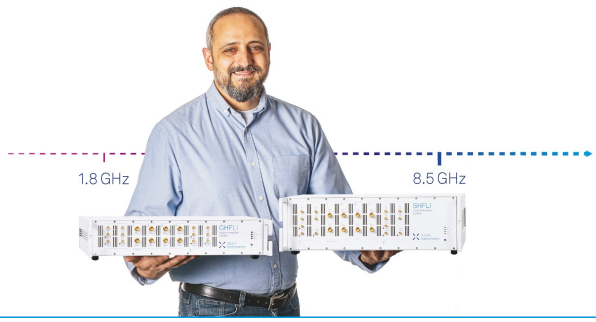
View Online Export Citation CrossMark

ARTICLES YOU MAY BE INTERESTED IN

TURBOMOLE: Modular program suite for ab initio quantum-chemical and condensed-matter simulations
The Journal of Chemical Physics **152**, 184107 (2020); https://doi.org/10.1063/5.0004635

The ORCA quantum chemistry program package
The Journal of Chemical Physics **152**, 224108 (2020); https://doi.org/10.1063/5.0004608

Spin contamination in MP2 and CC2, a surprising issue
The Journal of Chemical Physics **154**, 131101 (2021); https://doi.org/10.1063/5.0044362



Trailblazers. New
Meet the Lock-in Amplifiers that measure microwaves.
Zurich Instruments
Find out more

© 2022 Author(s).

AIP Publishing

The Journal of Chemical Physics ARTICLE scitation.org/journal/jcp

Pushing the limits: Efficient wavefunction methods for excited states in complex systems using frozen-density embedding

Cite as: J. Chem. Phys. 157, 204101 (2022); doi: 10.1063/5.0100393
Submitted: 24 May 2022 • Accepted: 31 October 2022 •
Published Online: 22 November 2022

View Online Export Citation CrossMark

Robert S. Treß,[1,a] Jing Liu,[2] Christof Hättig,[1] and Sebastian Höfener[2,b]

AFFILIATIONS

[1] Department of Theoretical Chemistry, Ruhr University Bochum, 44801 Bochum, Germany
[2] Institute of Physical Chemistry, Karlsruhe Institute of Technology (KIT), 76131 Karlsruhe, Germany

[a] **Author to whom correspondence should be addressed:** robert.tress@rub.de
[b] **Electronic mail:** hoefener@kit.edu

ABSTRACT

Frozen density embedding (FDE) is an embedding method for complex environments that is simple for users to set up. It reduces the computation time by dividing the total system into small subsystems and approximating the interaction by a functional of their densities. Its combination with wavefunction methods is, however, limited to small- or medium-sized molecules because of the steep scaling in computation time of these methods. To mitigate this limitation, we present a combination of the FDE approach with pair natural orbitals (PNOs) in the TURBOMOLE software package. It combines the uncoupled FDE (FDEu) approach for excitation energy calculations with efficient implementations of second-order correlation methods in the ricc2 and pnoccsd programs. The performance of this combination is tested for tetraazaperopyrene (TAPP) molecular crystals. It is shown that the PNO truncation error on environment-induced shifts is significantly smaller than the shifts themselves and, thus, that the local approximations of PNO-based wavefunction methods can without the loss of relevant digits be combined with the FDE method. Computational wall times are presented for two TAPP systems. The scaling of the wall times is compared to conventional supermolecular calculations and demonstrates large computational savings for the combination of FDE- and PNO-based methods. Additionally, the behavior of excitation energies with the system size is investigated. It is found that the excitation energies converge quickly with the size of the embedding environment for the TAPPs investigated in the current study.

Published under an exclusive license by AIP Publishing. https://doi.org/10.1063/5.0100393

I. INTRODUCTION

The computation of accurate excitation energies usually requires large and diffuse basis sets and accurate correlated electronic structure methods beyond time-dependent density functional theory (TDDFT) with semi-local functionals.[1] This can lead to enormous computation times for complex systems consisting of many molecules. Embedding methods can reduce the computation time by approximating the interactions of the surrounding molecules with the chromophore under study. For molecules in solution, continuum solvation models, such as the polarizable continuum model[2] (PCM), the conductor-like screening model[3] (COSMO), or the solvation model based on density[4] (SMD), are popular approaches. They require only a small amount of computational effort, but are limited in their applicability to situations where the description of the environment by a homogeneous continuum is sufficient. An alternative to continuum solvation models is to use a classical, i.e., molecular mechanics and electrostatic, description of the environment, which leads to the QM/MM and QM/MM-pol methods[5–7] as, e.g., the polarizable embedding[8–11] (PE) method. These methods require for each atom or atom type a number of parameters that need to be determined. Depending on the complexity of the environment and the details of the QM/MM or QM/MM-pol method, this can limit the accuracy and lead to complicated work flows that are often only worthwhile if used in repeated calculation, e.g., for geometry optimizations or MD trajectories.

The frozen density embedding (FDE) method avoids such parameterization steps, which makes its application to complex environments more straightforward. In the FDE method, the whole physical system is divided into subsystems that are treated sepa-

Published under an exclusive license by AIP Publishing

rately with quantum mechanical methods, and their interaction is described through their electron densities using in addition to the exact Coulomb interaction functionals for the kinetic, exchange, and correlation contributions to the interaction. For subsystems of equal size, the FDE embedding can achieve a linear scaling with the number of subsystems if combined with a fast multipole method for the Coulomb interaction. The FDE method was originally developed[12] as a partition scheme within density functional theory (DFT). Later, in addition to DFT-in-DFT approaches,[13] combinations with wavefunction theory (WFT) methods were also developed. A strict derivation of such WFT-in-DFT approaches was given by Wesołowski,[14] and implementations have been reported for, e.g., Hartree–Fock[15](HF), Møller–Plesset perturbation[16] (MPn) theory, configuration interaction[17] (CI), CASSCF, and coupled cluster (CC) methods.[18,19] While the FDE method is, in principle, exact, in practice, the kinetic and exchange–correlation functionals have to be approximated. In addition, the *v*-representability of the optimized density of a subsystem is not guaranteed through an interacting Hamiltonian.[20] One drawback of these approximations is that strong interactions between subsystems are usually not well described, which renders the division of a molecule into several subsystems unreasonable without further measures, such as introducing capping groups as in the 3-FDE scheme.[13] In addition, strong couplings between two close molecules can only be described within the coupled FDE (FDEc) method[21] so that for the uncoupled FDE (FDEu) method,[22] both molecules have to be considered as one subsystem. Those two cases can lead to subsystem sizes that no longer allow us to use conventional implementations of higher-order methods, such as coupled cluster (CC).

One way to reduce computation costs for CC methods is to reduce the virtual space by introducing pair natural orbitals (PNOs). During the generation of the PNOs, their contributions to the electron correlation energy[23,24] are estimated and PNOs with insignificant contributions are then neglected. This can lead to enormous reductions in computation time and storage requirements for large systems. Thus, PNO-CC methods are also an attractive option to overcome the problem that arises in FDE for large subsystems.

Multilevel HF and CC methods[25–29] are an alternative approach to reduce the computational costs for complex systems. Multilevel HF is a WFT-in-WFT method, which partitions in difference to FDE the density matrix of the full system, while multilevel CC allows for the computation of coupled cluster correlation contributions at different levels for different parts of the system. Similar to PNO-based CC methods, multilevel CC also requires a HF wavefunction of the whole (active) system.

In the current contribution, we present an extension of the FDE implementation[30] in the TURBOMOLE program package[31] for the calculation of excitation energies with the correlated second-order methods CIS(D), ADC(2), and CC2. The embedding potential can now be calculated using only the basis functions of the active subsystem, FDE calculations are no longer limited to two subsystems, the resolution of identity approximation can be used, and the OMP and MPI parallelization schemes implemented in TURBOMOLE can now be exploited. For correlated wavefunction and response calculations, the FDE implementation is combined with the ricc2 and pnoccsd programs[32–35] that exploit the resolution-of-the-identity (RI) and the PNO approximation to reduce the computational costs and storage requirements to allow for FDE calculations with larger subsystems than it would have been possible with conventional implementations.

In Sec. II, we give a brief review of the FDE approach and the combination with coupled cluster and response theory that is used for the current implementation, followed by a review of the approximations for the pair natural orbitals for the excitation energy. In Secs. III and IV, we give the computational details and discuss the results of benchmark calculations that have been carried out to analyze the performance of the implemented approach and, in particular, to calculate excitation energies of tetraazaperopyrenes (TAPPs) in their molecular crystals and compare wall times of FDE calculations with different subsystem sizes with those of supermolecular calculations for different sizes of the total computational models and investigate the convergence of the excitation energies with the size of the embedding environment.

II. THEORY AND IMPLEMENTATION

A. Frozen density embedding

The FDE method is based on subsystem DFT, where the total electron density is described as the sum of subsystem electron densities,[36–38]

$$\rho_{\mathrm{tot}}(\mathbf{r}) = \sum_{i=1}^{m} \rho_i(\mathbf{r}). \tag{1}$$

The total number of subsystems m is usually equal to the number of molecules in the investigated system. Using this decomposition of the total electron density leads to the following expression of the total energy:

$$E_{\mathrm{tot}} = \sum_{i=1}^{m} E_i[\rho_i] + E_{\mathrm{int}}[\rho_1(\mathbf{r}), \ldots, \rho_m(\mathbf{r})], \tag{2}$$

where $E_i[\rho_i(\mathbf{r})]$ is the energy expression of subsystem i and E_{int} is the interaction energy between the different subsystems. This decomposition has the advantage that each subsystem can, in general, be described with a different method and, in particular, also with wavefunction methods. In the latter case, the density functional $E_i[\rho_i]$ is for these subsystems replaced by the respective wavefunction functional $E_i[\Psi_i]$. The interaction contribution, however, is, nevertheless, also for these subsystems described through the electron densities. Employing wavefunction methods for all subsystems this leads to the following energy expression:

$$E_{\mathrm{tot}} = \sum_{i=1}^{m} E_i[\Psi_i] + E_{\mathrm{int}}[\rho_1(\mathbf{r}), \ldots, \rho_m(\mathbf{r})]. \tag{3}$$

This is motivated by the fact that, regardless of the methods chosen, the interaction is then determined only through the electron densities of the subsystems as

$$\begin{aligned} E_{\mathrm{int}}[\rho_1(\mathbf{r}), \ldots, \rho_m(\mathbf{r})] = {} & \sum_{i=1}^{m-1} \sum_{j>i}^{m} \int\int \frac{\rho_i(\mathbf{r})\rho_j(\mathbf{r}')}{|\mathbf{r}-\mathbf{r}'|} d\mathbf{r} d\mathbf{r}' + \sum_{i=1}^{m} \sum_{j\neq i}^{m} \\ & \times \int \rho_i(\mathbf{r}) v_N^j(\mathbf{r}) d\mathbf{r} + E_{\mathrm{kxc}}^{\mathrm{nadd}}[\rho_1(\mathbf{r}), \ldots, \rho_m(\mathbf{r})] \\ & + \sum_{i=1}^{m-1} \sum_{j>i}^{m} \sum_{A\in i} \sum_{B\in j} \frac{Z_A Z_B}{R_{AB}}, \end{aligned} \tag{4}$$

Published under an exclusive license by AIP Publishing

where, e.g., Z_A is the nuclear charge of atom A. R_{AB} is the distance between atoms A and B, and

$$v_N^j(\mathbf{r}) = \sum_{B\in j}\left(-\frac{Z_B}{|\mathbf{R}_B - \mathbf{r}|}\right) \tag{5}$$

is the nuclear potential of subsystem j, and $\mathbf{R}_B$ is the position of atom B. $E_{\mathrm{kxc}}^{\mathrm{nadd}}$ contains the nonadditive contributions of the kinetic and exchange–correlation energy, which is given as

$$E_{\mathrm{kxc}}^{\mathrm{nadd}}[\rho_1(\mathbf{r}),\ldots,\rho_m(\mathbf{r})] = T[\rho_1(\mathbf{r})+\cdots+\rho_m(\mathbf{r})] - \sum_{i=1}^{m} T[\rho_i(\mathbf{r})] + E_{\mathrm{xc}}[\rho_1(\mathbf{r})+\cdots+\rho_m(\mathbf{r})] - \sum_{i=1}^{m} E_{\mathrm{xc}}[\rho_i(\mathbf{r})]. \tag{6}$$

To keep $E_{\mathrm{kxc}}^{\mathrm{nadd}}$, an orbital free density functional that is free from any explicit information on the wavefunctions, the kinetic contributions must be computed with an explicit kinetic energy density functional. The derivation of the equations for the energy, or wavefunction, for a subsystem i leads now to the conventional, i.e., non-embedded, equations with a Hamiltonian augmented by an additional local potential that arises from the interaction energy. This additional potential is commonly denoted as embedding potential and is given by

$$v_{\mathrm{FDE}}^i(\mathbf{r}) = \sum_{j\neq i}^{m}\int \frac{\rho_j(\mathbf{r}')}{|\mathbf{r}-\mathbf{r}'|}d\mathbf{r}' + \sum_{j\neq i}^{m} v_{\mathrm{N}}^j(\mathbf{r}) + v_{\mathrm{kxc}}^i(\mathbf{r}), \tag{7}$$

where v_{kxc}^i contains the functional derivatives of the nonadditive contributions. As described in previous work,[39] additional all-electron pseudopotentials are added to the environment in order to account more completely for the Pauli repulsion between the electrons of a subsystem i and its embedding environment, leading to the following Fock operator:

$$F^{\mathrm{FDE(\,ECP)}} = F^{\mathrm{vac}} + v_{\mathrm{FDE}}^i + v_{\mathrm{ECP}}^i, \tag{8}$$

where F^{vac} is the Fock operator and v_{ECP}^i is the sum of the all-electron ECPs on all atoms of the environment for subsystem i, and to an additional contribution to the interaction energy, which consists of the sum of the expectation values of all subsystems i for the respective potentials v_{ECP}^i. Since in the current work the Fock operator always corresponds to the active subsystem i, the superscript is for notational simplicity here and in the following dropped. With that, the HF and, for DFT, the Kohn–Sham equations remain unchanged apart from using an augmented potential. For self-consistent field (SCF) methods, such as HF and DFT, the ground-state equations, that follow from the minimization of the total energy are solved self-consistently in freeze-and-thaw cycles.[40]

In our implementation, the embedding potential v_{FDE}^i is calculated from the electron densities and nuclear positions on a supermolecular integration grid that is generated by merging atom-centered integration grids for all atoms in the total system. The potentials are evaluated for each active subsystem only once at the beginning of a subsystem calculation, and the values of the density on the grid are updated after a converged SCF procedure in the so-called macroiterations. The integrals are evaluated only for the basis functions of the currently active subsystem.

The FDE extension is implemented within the dscf and ridft programs for HF and DFT employing OMP and MPI parallelization schemes and was validated by comparisons with the quantum chemistry software KOALA.[41]

Within the perturbation of the energy (PTE) reaction field scheme, where the embedding potential is kept fixed after self-consistency at the HF level is reached, no further changes to the code have to be made for post-Hartree–Fock ground state calculations.

As for other reaction field methods that allow for a polarization of the environment, one can devise for post-SCF methods, in particular in connection with response theory, different reaction field coupling schemes,[42–45] which have all their advantages and disadvantages for different applications. We use for the current implementation the post-SCF coupling scheme that in the ricc2 and pnoccsd programs of TURBOMOLE is also used for the PE and COSMO embeddings.[9,11,46]

In the post-SCF coupling scheme, the reaction field for the ground-state reference wavefunction is determined fully self-consistently with the reference wavefunction and its density. The post-SCF parts of the wavefunction, i.e., for coupled cluster and related methods, the amplitudes and Lagrange multipliers, are then determined in a reaction field that includes the respective contributions to the density. The post-SCF contributions to the density and the reaction field are, however, not fed back into the freeze-and-thaw cycles for the reference wavefunction. This reduces the costs relative to coupling schemes that determine all wavefunctions and densities in a reaction field that has been equilibrated with the post-SCF, e.g., coupled cluster density. However, equally important, this coupling scheme avoids a functional dependence of the reference wavefunction on post-SCF contributions to the density and thereby allows for a more consistent formulation of response and perturbation theories.

In the current work, we use FDEu where the response functions for each subsystem are decoupled by neglecting inter-system contributions. Within the post-SCF coupling scheme, this is consistent with determining the reaction field for post-SCF correlation and response calculations from the unperturbed self-consistent field reference densities of the environment and the full post-SCF density of the active subsystem that is currently under consideration.

B. FDE contributions in post-Hartree–Fock wavefunction methods

For the coupled cluster (CC) in the HF or DFT ansatz, we follow the derivation in Refs. 18 and 19 and use a variational formulation in terms of a Lagrangian. For simplicity, we restrict the equations to the closed-shell case and use the second quantization formalism. For an isolated system, the CC Lagrangian is given by

$$L(\bar{t}_\mu, t_\mu) = \langle \mathrm{HF}|H|\,\mathrm{CC}\rangle + \sum_\mu \bar{t}_\mu \langle\mu|\exp(-T)H|\,\mathrm{CC}\rangle = \langle\Lambda|H|\,\mathrm{CC}\rangle, \tag{9}$$

where $|\mathrm{CC}\rangle = \exp(T)|\mathrm{HF}\rangle$ is the CC wavefunction, $T = \sum_\mu t_\mu \tau_\mu$ is the cluster operator with the excitation operators τ_μ and amplitudes

Published under an exclusive license by AIP Publishing

t_μ, while $\langle\mu|$ is an element of the projection manifold, and $\bar{t}_\mu$ represent the Lagrange multipliers. The latter are combined with $\langle$HF| to $\langle\Lambda| = \langle\mathrm{HF}| + \sum_\mu t_\mu\langle\mu|$. Note that if the right-hand side of Eq. (9) becomes complex, only the real part should be used. The densities obtained from the above Lagrangian are the so-called "unrelaxed" coupled-cluster densities since they do not account for a response (relaxation) of the orbitals.

The Lagrangian for the total energy of the whole system takes the same form as the expression for the total energy in Eq. (3), but with $E_i[\Psi_i]$ replaced by L_i for those subsystems that are treated at the CC level. For simplicity, we use in the following for the active subsystem a lower index act and collect all other subsystems in the environment and write L_{tot} as the sum of the Lagrangian for the active system (L_{act}) and the sum of the Lagrangians for the subsystems in the environment (L_{env}) and the interaction contribution (E_{int}):[18,19]

$$L_{\mathrm{tot}} = L_{\mathrm{act}} + L_{\mathrm{env}} + E_{\mathrm{int}}. \tag{10}$$

For FDEu with the post-SCF coupling scheme, the interaction energy is for the coupled cluster and response part of the calculations defined as $E_{\mathrm{int}}[\rho^{\mathrm{CC}}_{\mathrm{act}}, \rho^{\mathrm{SCF}}_{\mathrm{env}}]$, where ρ^{SCF}_i can be a Hartree–Fock or DFT density and $\rho^{\mathrm{CC}}_{\mathrm{act}}$ is the (unrelaxed) coupled cluster density obtained from the coupled cluster Lagrangian, Eq. (9), of the active system. The CC amplitude equations for the embedded system are obtained from the stationarity condition for the total Lagrangian, Eq. (10), with respect to the Lagrange multipliers,

$$0 = \frac{\delta L}{\delta \bar{t}_{\mu_i}} = \Omega^{\mathrm{vac}}_{\mu_i} + \sum_{pq}\langle p|v_{\mathrm{int}}|q\rangle\langle\mu_i|\exp(-T)E_{pq}|\,\mathrm{CC}\rangle, \tag{11}$$

with $\Omega^{\mathrm{vac}}_{\mu_i}$ as the vacuum contribution to the residual of the amplitude equations and

$$v_{\mathrm{int}}[\rho^{\mathrm{CC}}_{\mathrm{act}}, \rho^{\mathrm{SCF}}_{\mathrm{env}}] = v^i_{\mathrm{FDE}}[\rho^{\mathrm{CC}}_{\mathrm{act}}, \rho^{\mathrm{SCF}}_{\mathrm{env}}] + v^i_{\mathrm{ECP}}. \tag{12}$$

At this point, we introduce the reaction field operator,

$$G = \sum_{pq}\langle p|v_{\mathrm{int}}|q\rangle E_{pq}, \tag{13}$$

and we write Eq. (11) as

$$0 = \frac{\delta L}{\delta \bar{t}_{\mu_i}} = \Omega^{\mathrm{vac}}_{\mu_i} + \langle\mu_i|\exp(-T)G|\,\mathrm{CC}\rangle. \tag{14}$$

The contributions arising from G are straightforward to evaluate as they have the same structure as the contributions arising from the Fock operator in the amplitude equations for an isolated system.

Similarly, the Lagrange multipliers are obtained from the stationarity condition of the total Lagrangian with respect to the amplitudes,

$$0 = \frac{\delta L}{\delta t_{\mu_i}} = \langle\Lambda|[H, \tau_{\mu_i}]|\,\mathrm{CC}\rangle + \langle\Lambda|[G, \tau_{\mu_i}]|\,\mathrm{CC}\rangle. \tag{15}$$

In response theory for isolated systems, excitation energies are usually derived as poles of the response functions. This can, in principle, also be done for subsystem formulations. However, similar to other embedding approaches with polarizable environments, the contributions to the Lagrangian arising from the interaction contributions that are quadratic in the multipliers introduce an additional coupling between the cluster amplitudes and the multipliers.[18] As a consequence, the poles no longer occur at the eigenvalues of the CC Jacobian, but at the eigenvalues of the full electronic Hessian with the amplitudes and multipliers considered as variables on equal footing. This leads to significant computational overhead, while the numerical effects on excitation energies are expected to be small. We thus follow the computational strategy that has been successfully employed in the CC/MM schemes[47] and the related PE-CC and PCM- and COSMO-CC approaches[45,48–50] and neglect this coupling and determine the excitation energies of the embedded system as eigenvalues of its Jacobian. From the definition of the Jacobian,

$$A_{\mu_i\nu_j} = \frac{\delta^2 L_{\mathrm{tot}}}{\delta\bar{t}_{\mu_i}\delta t_{\nu_j}} = A^{\mathrm{vac}}_{\mu_i\nu_j} + A^{\mathrm{FDE}}_{\mu_i\nu_j}, \tag{16}$$

one obtains with the above choice for E_{int} for the FDE contribution,

$$A^{\mathrm{FDE}}_{\mu_i\nu_j} = \langle\mu_i|\big[G, \tau_{\nu_j}\big]|\,\mathrm{CC}\rangle + \frac{1}{2}\sum_{pq,rs}(pq|\omega_{\mathrm{int}}|rs) \times \langle\mu_i|\exp(-T)E_{pq}|\,\mathrm{CC}\rangle\langle\Lambda|[E_{rs}, \tau_{\nu_j}]|\,\mathrm{CC}\rangle. \tag{17}$$

The second term includes the so-called kernel contributions, which received their name due to their analogy to the exchange–correlation kernel in DFT-based response theory,

$$(pq|\omega_{\mathrm{int}}|rs) = \iint\phi^\dagger_p(\mathbf{r}')\phi_q(\mathbf{r}')\left[\left.\frac{\delta^2 E_{\mathrm{kxc}}}{\delta\rho(\mathbf{r}')\delta\rho(\mathbf{r})}\right|_{\rho_{\mathrm{tot}}} - \left.\frac{\delta^2 E_{\mathrm{kxc}}}{\delta\rho(\mathbf{r}')\delta\rho(\mathbf{r})}\right|_{\rho_{\mathrm{act}}}\right] \times \phi^\dagger_r(\mathbf{r})\phi_s(\mathbf{r})d\mathbf{r}d\mathbf{r}'. \tag{18}$$

The excitation energies for the active subsystem are obtained by solving the right eigenvalue for the Jacobian,

$$\mathbf{A}\mathbf{R}_k = \omega_k\mathbf{R}_k. \tag{19}$$

C. The second-order methods CC2, ADC(2), and CIS(D)

The approximate coupled-cluster singles and doubles model CC2 was introduced[51] as an approximation to the coupled-cluster singles and doubles model CCSD where the iterative character of coupled cluster is retained, but only terms that are at most of second order are kept in the Lagrangian. For this truncation, the electron fluctuation potential, $W = H - F$, and the doubles amplitudes and multipliers are as in Møller–Plesset perturbation theory, counted as first order. Due to their special role in response theory, the singles amplitudes and multipliers are treated as being of zeroth-order. This leads to the Lagrangian

$$\begin{aligned} L^{\mathrm{CC2}} = {} & \langle\mathrm{HF}|H\,\exp(T)|\mathrm{HF}\rangle \\ & + \sum_{\mu_1}\bar{t}_{\mu_1}\langle\mu_1|\exp|(-T_1)(H + [H, T_2])\exp(T_1)|\mathrm{HF}\rangle \\ & + \sum_{\mu_2}\bar{t}_{\mu_2}\langle\mu_2|\exp(-T_1)H\exp(T_1) + [F, T_2]|\mathrm{HF}\rangle. \end{aligned} \tag{20}$$

Published under an exclusive license by AIP Publishing

The CC2 model gives ground-state and excitation energies for single excitations that are complete through second-order in the fluctuation potential.

For FDE, the second-order approximation must be generalized to the interaction contribution in the Lagrangian. In this context, the intersystem electron–electron interaction should in the perturbation expansion be treated similar to the intrasystem electron–electron interactions. A natural choice is to count the interaction potential that arises from the SCF densities as being of zeroth order, on equal footing with the Coulomb and exchange contributions in the vacuum Fock matrix, and all intersystem electron–electron interactions in contributions beyond the mean field potential as being of first order. In case of CC2, the unrelaxed density matrix[51] given as

$$\begin{aligned} D_{pq}^{\mathrm{CC2}} &= \langle \mathrm{HF}| \exp(-T_1) E_{pq} \exp(T_1) |\mathrm{HF}\rangle \\ &+ \sum_{\mu_1} \bar{t}_{\mu_1} \langle \mu_1| \exp(-T_1)(E_{pq} + [E_{pq}, T_2]) \exp(T_1) |\mathrm{HF}\rangle \\ &+ \sum_{\mu_2} \bar{t}_{\mu_2} \langle \mu_2| \exp(-T_1)[E_{pq}, T_2] \exp(T_1) |\mathrm{HF}\rangle \end{aligned} \tag{21}$$

depends on the doubles multipliers and doubles amplitudes in the last term, which is, therefore, of second order, and gives in the interaction contribution to L_{tot} only rise to contributions that are of third order and beyond that are not consistent with a second-order model. As discussed in Ref. 9 in the framework of polarizable embedding, the contribution to D^{CC2} that is proportional to the doubles amplitudes and singles multipliers also introduces in reaction field approaches contributions beyond second order and causes for a consistent second-order model complications. It is, therefore, skipped for CC2. The interaction term is thus in the post-SCF coupling scheme for CC2 evaluated with a CCS-like density matrix, which includes in addition to the Hartree–Fock term only contributions from the singles amplitudes and multipliers, which are taken from the FDE-CC2 calculation,

$$\begin{aligned} D_{pq}^{\mathrm{CCS}} &= \langle \mathrm{HF}| \exp(-T_1) E_{pq} \exp(T_1) |\mathrm{HF}\rangle \\ &+ \sum_{\mu_1} \bar{t}_{\mu_1} \langle \mu_1| \exp(-T_1) E_{pq} \exp(T_1) |\mathrm{HF}\rangle. \end{aligned} \tag{22}$$

The total energy Lagrangian for CC2 in HF or DFT thus becomes

$$L_{\mathrm{tot}} = L_{\mathrm{act}}^{\mathrm{CC2}} + E_{\mathrm{int}}[\rho_{\mathrm{act}}^{\mathrm{CCS}}, \rho_{\mathrm{env}}^{\mathrm{SCF}}] + L_{\mathrm{env}}^{\mathrm{SCF}}. \tag{23}$$

This leads to the following amplitude equations:

$$0 = \langle \mu_1| \exp(-T_1) \left(H^{\mathrm{emb}} + \left[H^{\mathrm{emb}}, T_2 \right] + G^{\Delta} \right) \exp(T_1) |\mathrm{HF}\rangle, \tag{24}$$

$$0 = \langle \mu_2| \exp(-T_1) H^{\mathrm{emb}} \exp(T_1) + \left[F^{\mathrm{emb}}, T_2 \right] |\mathrm{HF}\rangle, \tag{25}$$

with

$$\begin{aligned} G^{\Delta} &= G - G^{\mathrm{SCF}} = \sum_{pq} \langle p| v_{\mathrm{int}}[\rho_{\mathrm{act}}^{\mathrm{CCS}}, \rho_{\mathrm{env}}^{\mathrm{SCF}}] - v_{\mathrm{int}}[\rho_{\mathrm{act}}^{\mathrm{SCF}}, \rho_{\mathrm{env}}^{\mathrm{SCF}}] |q\rangle E_{pq} \\ &= \sum_{pq} \langle p| v_{\mathrm{kxc}}^{\mathrm{nadd}}[\rho_{\mathrm{act}}^{\mathrm{CCS}}, \rho_{\mathrm{env}}^{\mathrm{SCF}}] - v_{\mathrm{kxc}}^{\mathrm{nadd}}[\rho_{\mathrm{act}}^{\mathrm{SCF}}, \rho_{\mathrm{env}}^{\mathrm{SCF}}] |q\rangle E_{pq}, \end{aligned} \tag{26}$$

where G^{SCF} is the SCF reaction field operator calculated from the SCF densities. In Eqs. (24) and (25), we included the SCF reaction field in F^{emb} and H^{emb}, which are defined as the respective vacuum operators plus the SCF interaction potential,

$$F^{\mathrm{emb}} = F^{\mathrm{vac}} + v_{\mathrm{int}}[\rho_{\mathrm{act}}^{\mathrm{SCF}}, \rho_{\mathrm{env}}^{\mathrm{SCF}}]. \tag{27}$$

This is motivated by the fact that the SCF reaction field is included via the Fock matrix obtained from the preceding FDE calculation at the HF or DFT level. In the post-SCF part, F^{emb} remains unchanged, and only G^{Δ} depends on the cluster amplitudes and Lagrange multipliers. We note that in the equation for the doubles amplitudes, Eq. (25), in the first term on the right-hand side from $H^{\mathrm{emb}} = F^{\mathrm{emb}} + W$ only the electron fluctuation potential W contributes.

The equations for the Lagrange multipliers become

$$\begin{aligned} 0 &= \langle \mathrm{HF}| \left[H^{\mathrm{emb}} + G^{\Delta}, \tau_{\mu_1} \right] \exp(T) |\mathrm{HF}\rangle + \sum_{\mu_1} \bar{t}_{\mu_1} \langle \mu_1| \exp(-T_1) \\ &\times \left(\left[H^{\mathrm{emb}} + G^{\Delta}, \tau_{\mu_1} \right] + \left[\left[H^{\mathrm{emb}}, T_2 \right], \tau_{\mu_1} \right] \right) \exp(T_1) |\mathrm{HF}\rangle \\ &+ \sum_{\mu_2} \bar{t}_{\mu_2} \langle \mu_2| \exp(-T_1) \left[H^{\mathrm{emb}}, \tau_{\mu_1} \right] \exp(T_1) |\mathrm{HF}\rangle \end{aligned} \tag{28}$$

and

$$\begin{aligned} 0 &= \langle \mathrm{HF}| \left[H^{\mathrm{emb}}, \tau_{\mu_2} \right] \exp(T) |\mathrm{HF}\rangle + \sum_{\mu_1} \bar{t}_{\mu_1} \langle \mu_1| \exp(-T_1) \left[H^{\mathrm{emb}}, \tau_{\mu_2} \right] \\ &\times \exp(-T_1) |\mathrm{HF}\rangle + \sum_{\mu_2} \bar{t}_{\mu_2} \langle \mu_2| \left[F^{\mathrm{emb}}, \tau_{\mu_2} \right] |\mathrm{HF}\rangle. \end{aligned} \tag{29}$$

With the restriction to the CCS-like density for the interaction energy, for the Jacobian explicit contributions from the embedding beyond those automatically included via F^{emb} arise only in the singles–singles block,

$$\begin{aligned} A_{\mu_1 \nu_1}^{\mathrm{FDE}} &= \langle \mu_1| \exp(-T_1) \left[\left(H^{\mathrm{emb}} + \left[H^{\mathrm{emb}}, T_2 \right] + G^{\Delta} \right), \tau_{\nu_1} \right] \exp(T_1) |\mathrm{HF}\rangle \\ &+ \sum_{pqrs} (pq| \omega_{\mathrm{int}}^{\mathrm{CCS}} |rs) \langle \Lambda_1| [E_{rs}, \tau_{\nu_1}] \exp(T_1) |\mathrm{HF}\rangle \langle \mu_1| \exp(-T_1) \\ &\times E_{pq} \exp(T_1) |\mathrm{HF}\rangle. \end{aligned} \tag{30}$$

The eigenvalue problem for the excitation energies, Eq. (19), is solved using iterative direct techniques, which only needs the possibility to compute contractions of $\mathbf{A}$ with trial vectors $\mathbf{b}$. For the FDE contributions, this is implemented by first setting up a transition density,

$$\rho^b(\mathbf{r}) = \sum_{rs} \phi_r^{\dagger}(\mathbf{r}) \phi_s(\mathbf{r}) D_{rs}^b, \tag{31}$$

$$\mathbf{D}^b = \begin{pmatrix} -\bar{\mathbf{t}}_1^{\dagger} \mathbf{b}_1 & 0 \\ 2\mathbf{b}_1 & \bar{\mathbf{t}}_1 \mathbf{b}_1^{\dagger} \end{pmatrix}, \tag{32}$$

which is then used to evaluate the integrals on the supermolecular grid,

Published under an exclusive license by AIP Publishing

$$G^b_{\mu\nu} = \int \chi_\mu(\mathbf{r}')\chi_\nu(\mathbf{r}') \times \int \left[\left. \frac{\delta^2 E_{\mathrm{kxc}}}{\delta\rho(\mathbf{r}')\delta\rho(\mathbf{r})} \right|_{\rho_{\mathrm{tot}}} - \left. \frac{\delta^2 E_{\mathrm{kxc}}}{\delta\rho(\mathbf{r}')\delta\rho(\mathbf{r})} \right|_{\rho_{\mathrm{act}}} \right] \rho^b(\mathbf{r}) d\mathbf{r} d\mathbf{r}', \quad (33)$$

for the atomic orbitals χ_μ. These integrals are then transformed to the molecular orbital basis, which allows us to formulate the FDE contribution to $\boldsymbol{\sigma} = \mathbf{Ab}$ as

$$\sigma^{\mathrm{FDE}}_{\mu_1} = \sum_{\nu_1} A^{\mathrm{FDE}}_{\mu_1\nu_1} b_{\nu_1} = \langle \mu_1 | \exp(-T_1) \left(\left[G^\Delta, b_1 \right] + G^b \right) \exp(T_1) | \mathrm{HF} \rangle, \quad (34)$$

with the one-electron operators $b_1 = \sum_{ab} b_{ai} E_{ai}$ and $G^b = \sum_{pq} G^b_{pq} E_{pq}$. The latter equation is evaluated similar to other one-electron contributions.

The algebraic diagrammatic construction is a propagator approach,[52] which uses a very different theoretical framework for the derivation of response functions than it is used in coupled cluster response theory. At the second-order level,[53] ADC(2), the secular matrix from which the excitation energies are obtained as eigenvalues is, however, technically closely related to that for the iterative variant of the configuration interaction singles model with a second-order doubles correction,[54] CIS(D$_\infty$), and the Jacoby matrix for CC2:[55] The secular matrix for CIS(D$_\infty$) is obtained by replacing in the CC2 Jacoby matrix the CC2 ground-state singles and doubles amplitudes by those from first-order Møller–Plesset perturbation theory. Similar to the CC2 Jacobian, it is non-Hermitian. The secular matrix for ADC(2) is equal to the Hermitian part of that for CIS(D$_\infty$).

The excitation energies for configuration interaction singles, CIS, with a perturbative second-order doubles correction,[56] CIS(D), can be written as

$$\omega^{\mathrm{CIS(D)}} = \mathbf{E}_1^{\mathrm{CIS}} \left(\mathbf{A}_{11}^{\mathrm{CIS(D_\infty)}} - \mathbf{A}_{12}^{\mathrm{CIS(D_\infty)}} \left[\mathbf{A}_{22}^{\mathrm{CIS(D_\infty)}} - \omega^{\mathrm{CIS}} \mathbf{1}_{22} \right]^{-1} \times \mathbf{A}_{21}^{\mathrm{CIS(D_\infty)}} \right) \mathbf{E}_1^{\mathrm{CIS}}, \quad (35)$$

where ω^{CIS} and $\mathbf{E}^{\mathrm{CIS}}$ are the CIS eigenvalues and eigenvectors and $\mathbf{A}_{kl}^{\mathrm{CIS(D_\infty)}}$ represent the respective blocks of the CIS(D$_\infty$) secular matrix for the excitation classes k, l. Note that for excitation energies, CIS is equivalent to coupled cluster singles, CCS, if the reference wavefunction fulfills the Brillouin condition.

The same relations can be used to derive from the FDE expressions for CC2 in HF or DFT the respective expressions for ADC(2), CIS(D$_\infty$), and CIS(D). All three methods require the ground-state amplitudes from first-order Møller–Plesset perturbation theory. The post-SCF coupling scheme used in the current work becomes at this level identical with the PTE scheme. The first-order singles amplitudes vanish, and the first-order doubles amplitudes are determined by the following equation:

$$0 = \langle \mu_2 | [F^{\mathrm{emb}}, T_2^{(1)}] + W | \mathrm{HF} \rangle. \quad (36)$$

The last equation differs from Eq. (25) only in that the fluctuation potential is not similarity-transformed with $\exp(T_1)$.

D. Pair natural orbital approximation of excitation energies

The implementation of the CIS(D) excitation energies with pair natural orbitals was described in Ref. 33, and its extension to the iterative methods ADC(2) and CC2 was described in Ref. 34. Here, only a brief summary on the use of the pair natural orbitals in the calculation of excitation energies is given.

The second-order methods for excitation energies have in common that the computationally most costly steps are related to the doubles amplitudes for the ground (t_{μ_2}) and excited states (E_{μ_2}) and two-electron integrals of the type $(ai|bj)$ with two occupied (i, j) and two virtual (a, b) MO indices, where the orbitals can be dressed with ground- and/or excited-states singles amplitudes. For localized occupied molecular orbitals (LMOs), the latter integrals are only non-negligible if the virtual MOs a and b are close to the LMOs i and j and their magnitude decays as R^{-3} with the distance between the centers of i and j.

This sparsity is exploited in the pair natural orbital approximation by determining for each LMO pair ij a set of PNOs that are defined as linear combinations of virtual orbitals,

$$|\bar{a}\rangle = \sum_a |a\rangle d^{ij}_{a\bar{a}}, \quad (37)$$

with the coefficient $d^{ij}_{a\bar{a}}$ chosen such that they diagonalize the correlation contribution D^{ij} of pair ij to the one-electron density matrix,

$$\sum_{ab} d^{ij}_{a\bar{a}} D^{ij}_{ab} d^{ij}_{b\bar{b}} = n^{ij}_{\bar{a}} \delta_{\bar{a}\bar{b}}, \quad (38)$$

with

$$D^{ij}_{ab} = \frac{2}{N_{ij}} \sum_c \left(u^{ij}_{ac} t^{ij}_{bc} + u^{ij}_{ca} t^{ij}_{cb} \right), \quad (39)$$

$$N_{ij} = 1 + \frac{2}{1 + \delta_{ij}} \sum_{ab} u^{ij}_{ab} t^{ij}_{ab}, \quad (40)$$

$$u^{ij}_{ab} = 2t^{ij}_{ab} - t^{ij}_{ba}, \quad (41)$$

and t^{ij}_{ab} as the MP2 doubles amplitudes. The eigenvalues $n^{ij}_{\bar{a}}$ are natural orbital occupation numbers and provide a measure for the importance of the corresponding PNO. Thus, all PNOs with a natural occupation number lower than a chosen PNO threshold value T_{PNO} are discarded. For localized LMOs ij, $n^{ij}_{\bar{a}}$ decay rapidly with the index $\bar{a}$ toward zero, which then leads to a large reduction of the virtual space for ij. In the second-order correlation methods CIS(D), ADC(2), and CC2, the double amplitudes are then used only within the PNO basis, and the integrals in which they are contracted are also projected onto it.

For the excited-state doubles amplitudes, a state-specific PNO basis is constructed for each excited state to account for the different characters of the excitations, which can be localized on a single chromophore group or exhibit long-range charge-transfer character in the case of non-local excitation. The excited state PNOs are obtained by a similar procedure as for the ground-state but with t^{ij}_{ab} replaced by the first order excited-state doubles amplitudes[33] E^{ij}_{ab},

Published under an exclusive license by AIP Publishing

$$\tilde{D}^{ij}_{ab} = \frac{2}{\tilde{N}_{ij}} \sum_{c} \left(\tilde{u}^{ij}_{ac} E^{ij}_{bc} + \tilde{u}^{ij}_{ca} t^{ij}_{cb} \right). \quad (42)$$

For further technical details on the generation of the PNO coefficients with a reduced scaling of the operation count with the system size and the truncation of the set of significant LMO pairs, we refer to Refs. 33–35.

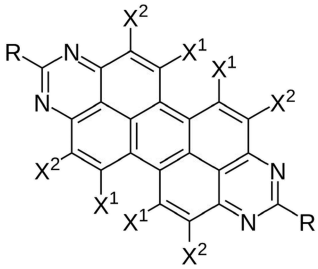
All FDE contributions have also been implemented within the pnoccsd program and have been tested by comparisons to the ricc2 program in the limit of a very tight PNO truncation threshold. With that, FDE is available in the pnoccsd program within the frozen density approximation and the post-SCF reaction field scheme in combination with PNOs.

III. COMPUTATIONAL DETAILS

A. Geometries

To test the performance of the FDE implementation, clusters were created from tetraazaperopyrene (TAPP) molecular crystals. The general structure of the TAPPs is shown in Fig. 1 together with the TAPP derivatives used for the current study.

The starting points for constructing the TAPP clusters were solid-state geometries for selected TAPP compounds available in the Cambridge Crystallographic Data Center (CCDC). We have used the CCDC entries 747 374 (Refs. 57 and 58) and 1 980 431 (Refs. 59 and 60) in the case of H-TAPP-H and *all*-C_3F_7-TAPP-Cl_4Br_4, respectively. In the case of monoclinic *bay*-C_2F_5-TAPP-H_4F_4, the structure from CCDC entry 1 908 781 (Refs. 61 and 62) is used in which the chlorine atoms are replaced with fluorine atoms. Starting from these initial geometries, the bulk phase was optimized using the CP2K program[63] with periodic DFT methods. Both the cell parameters and the crystal structures have been optimized with the PBE functional[64,65] and the TZVP-MOLOPT-GTH[66] basis set together with the GTH-PBE pseudopotential.[67] The DFT-D3 correction has been applied to account for dispersion.[68] Based on the fully optimized bulk phases, the clusters have been extracted using Avogadro[69] and VMD[70] such that only those molecules are included, which are entirely located within a specified radius. A detailed analysis for a broad range of TAPP compounds, including cell structure or electronic gaps and crystal stability, will be published elsewhere.[71]



Compound	X^1	X^2	R
(**1**) H-TAPP-H	H	H	H
(**2**) *bay*-C_2F_5-TAPP-H_4F_4	F	H	C_2F_5
(**3**) *all*-C_3F_7-TAPP-Cl_4Br_4	Cl	Br	C_3F_7

FIG. 1. Chemical structure of the investigated TAPP compounds.

With this method, clusters have been created with a radii of 8, 10, 12, and 15 Å for compound (1), with radii of 10, 12, 15, and 20 Å for compound (2), and with radii of 10, 13, 15, and 20 Å for compound (3) around a single central molecule. Additional clusters have been created for compounds (2) and (3) with radii of 10, 15, and 20 Å around a dimer of two stacked molecules. The largest clusters of each compound are shown in Fig. 2.

In addition to the TAPPs, two systems from previous work[39] are used to investigate the influence of the post-SCF kernel contributions on excitation energies: a Green Fluorescence Protein (GFP) model system with a non-covalently bound chromophore and 2,3-Diazabicyclo[2.2.2]oct-2-en (DBO) within Cucurbit[7]uril (CB[7]), both shown in Fig. 3. The structures of these two systems are taken from Ref. 72.

B. FDE and excitation energy calculations

All FDE and excitation energy calculations were carried out with a development version of the TURBOMOLE program package.[31] For all TAPP systems, we used the def2-TZVP basis set[73,74] for the atoms of the central molecule and the def2-SVP basis set[73,74] for the molecules in the environment. The def2-TZVP basis set[73,74] for the atoms in the central molecule was chosen based on test calculations (see the supplementary material) of an isolated molecule of compound (1), which showed that this basis is sufficient for excitation energies. The resolution of identity approximation for the Coulomb potential,[75] RI-J, was employed for all environment subsystems and for supermolecular calculations using the respective

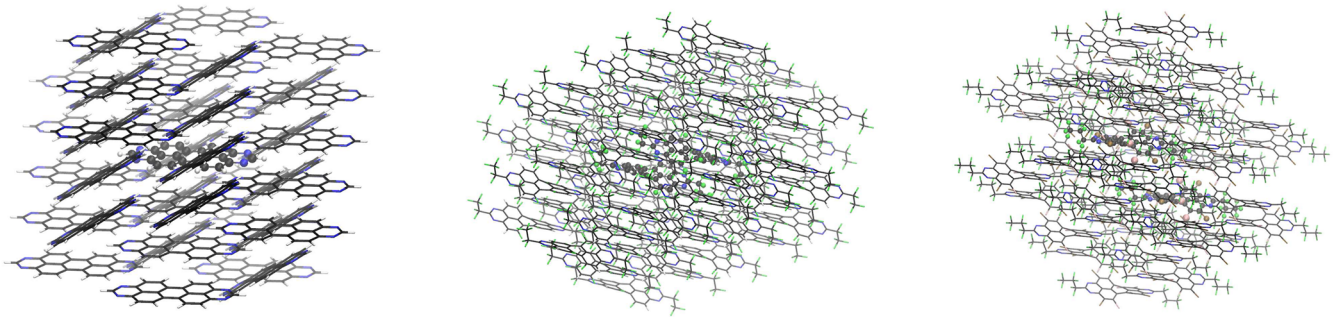


FIG. 2. Structures of the largest extracted clusters for each TAPP. (a) H-TAPP-H, (b) *bay*-C_2F_5-TAPP-H_4F_4, and (c) *all*-C_3F_7-TAPP-Cl_4Br_4.

Published under an exclusive license by AIP Publishing

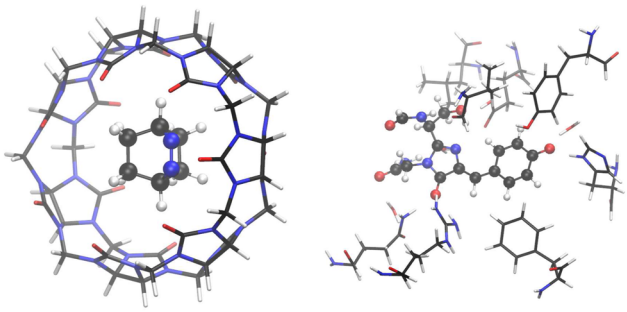


FIG. 3. Structures of systems used to investigate post-SCF kernel contributions. The examined chromophore is displayed with balls and sticks, while the environment is displayed as licorice. (a) DBO/CB7; (b) GFP.

optimized auxiliary basis sets from Ref. 74. For the current study, the first step is a self-consistent FDE calculation with all subsystems treated at the Hartree–Fock level. Here, for each subsystem, the respective monomer basis was used and the embedding potential was calculated with the PBE exchange–correlation[64] and revAPBEk kinetic energy functionals[76] on a supermolecular integration grid constructed from the atomic integration grids of all atoms using grid size 3 of the TURBOMOLE package. In addition, the all-electron pseudopotentials[72] ecp-all have been used to prevent electron spill-out effects,[39] and in the following, we will refer to this FDE(ECP) approach only as FDE. The freeze and thaw iterations have been carried out until the electronic energies of all subsystems were converged within a threshold of $5.0 \cdot 10^{-6}$ H. All post-Hartree–Fock calculations used for the resolution-of-the-identity approximations in the correlation contributions and the excitation energy calculations the respective auxiliary basis sets from Ref. 77. The frozen core approximation has been applied for all orbitals with energies below −3.0 hartree. All PNO-based calculations were performed with a PNO truncation threshold of 10^{-8} based on the results in Ref. 34 and test calculations of an isolated molecule of compound (1) (see the supplementary material) and used intrinsic bond orbital (IBO) localization for the occupied orbitals.[78]

IV. RESULTS

A. Evaluation of the post-SCF kernel contributions

Post-SCF contributions originate from a non-linear dependence of the embedding potential on the electron density in the active subsystem. Therefore, this contributions should be larger when the distances between the active and surrounding subsystems are small, resulting in an increased overlap of subsystem electron densities. To evaluate their importance, we computed post-SCF contributions for a GFP model system and for DBO within CB[7], as shown in Fig. 3. The GFP model system has been chosen because of the hydrogen bonds between the subsystems and also because of the, in general, small distances between them, and the DBO in the CB[7] system was found in previous studies[11,72] to be sensitive to electron charge spill-out in electronically excited states, which then causes a strong interaction between the subsystems. Therefore, excitation energies have been computed for the first two excitations within the CCS, ADC(2), and CC2 model using either the PTE or the post-SCF reaction field scheme together with the frozen solvent[79] approximation. For these systems, the aug-cc-pVTZ basis[80] for the chromophore and the cc-pVDZ basis[81] for the environment were used together with the lc94 kinetic energy functional[82] for the embedding potential.

As shown in Tables I and II, the post-SCF contributions are, in general, rather small. In the case of DBO in CB[7], the largest post-SCF kernel contribution is only 0.88 meV for the first excitation within the CC2 model, which is negligible. For the GFP model system, a post-SCF kernel contribution of 13.65 meV is observed for the second excitation within the CCS model, which shows that the post-SCF kernel contributions can be significant. However, for ADC(2) and CC2, the post-SCF kernel contributions of the same excitation are significantly lower.

To compare the FDE approach used in this work with a QM/MM alternative, we have computed the excitation energies with the PE(ECP) method within the PTE reaction field scheme for DBO in CB[7] and the GFP model system. The PE potentials were taken from Refs. 39 and 72. The detailed results can be found in the supplementary material. They reveal that the difference in the excitation energies between the two embedding models, i.e., PE and FDE, is more pronounced than the contributions of the post-SCF kernel. To give an example, while the latter are for the second excitation energy of the DBO in CB[7] ~0.7 meV in the case of the CC2 method, the difference between PE(ECP) and FDE(ECP) is −400 meV, being the same order of magnitude as the environment-induced shift of 558 meV. Employing ADC(2), which can be compared with the subsystem-ADC(2) results of Ref. 39, the error of −322 meV of the PE(ECP) method is reduced to −18 meV with the FDE(ECP) method.

Since the TAPPs that are studied in the following do not exhibit hydrogen bonds between the molecules, only insignificant contributions from the post-SCF scheme are expected. To check this

TABLE I. The first two excitation energies ω within the PTE model of the GFP model system and the additional post-SCF kernel contributions to the excitation energy $\Delta\omega$ for various methods. All in eV.

	CCS		ADC(2)		CC2	
	ω	$\Delta\omega$	ω	$\Delta\omega$	ω	$\Delta\omega$
S_1	3.661	$0.66 \cdot 10^{-3}$	2.487	$+0.36 \cdot 10^{-3}$	2.778	$+0.65 \cdot 10^{-3}$
S_2	4.552	$13.65 \cdot 10^{-3}$	2.774	$+0.07 \cdot 10^{-3}$	3.023	$+0.22 \cdot 10^{-3}$

Published under an exclusive license by AIP Publishing

TABLE II. The first two excitation energies ω within the PTE model DBO/CB[7] system and the additional post-SCF kernel contributions to the excitation energy $\Delta\omega$ for various methods. All in eV.

	CCS		ADC(2)		CC2	
	ω	$\Delta\omega$	ω	$\Delta\omega$	ω	$\Delta\omega$
S_1	3.683	$0.64 \cdot 10^{-3}$	3.437	$+0.78 \cdot 10^{-3}$	3.471	$+0.88 \cdot 10^{-3}$
S_2	6.711	$0.38 \cdot 10^{-3}$	6.106	$+0.63 \cdot 10^{-3}$	6.106	$+0.73 \cdot 10^{-3}$

presumption, we computed the post-SCF kernel contributions for compound (2). For most excitations, they are below 1 meV; the largest contribution obtained is 3.47 meV for the 14th excitation.

Since the post-SCF kernel contributions to the excitations of interest are only minor for the TAPPs, we decided to employ the PTE model with the frozen solvent approximation in the following.

B. PNO truncation error in FDE calculations

A major task of embedding methods in the framework of theoretical spectroscopy is to model environment-induced shifts in the spectra. These shifts are often small, so it is necessary to be careful that an approximation such as the truncation of the PNOs does not introduce errors in these shifts that are larger than the shifts themselves. In order to ensure that PNO-based methods are able to qualitatively describe environment-induced shifts for electronic valence excitations, the PNO truncation error on the environment shift was investigated for CC2. For ADC(2), the PNO truncation errors are, in general, similar to those for CC2, while they are usually a bit smaller for the perturbative CIS(D) method.

For these tests, the first four excitation energies of the isolated molecule and the molecule within the environment were computed with and without the PNO approximation for compounds (1) and (2) within the CC2 model. The clusters with radii of 15 Å for compound (1) and 20 Å for compound (2) around the target molecule were in these calculations used to model the environment.

For compound (2), we can see in Table III that the PNO truncation errors on the excitation energies increase with the excitation energy and reach for S_4 a value of 59.21 meV. The environment-induced shift for the first two excitations is relatively small, below 0.1 eV, so that the PNO truncation errors on the excitation energies are even slightly larger than the environment shifts. However, most of the PNO truncation errors consists of a mostly systematic blue shift, and thus, the PNO truncation error on the environment shift is, nevertheless, much smaller than the environment shift itself, in most cases by an order of magnitude.

For compound (**1**), the truncation errors on the excitation energies (see Table IV) are lower than the environment-induced shifts and the effects of the PNO truncation on the environment shifts are also for this compound much smaller than the shifts themselves. For the first excitation energy, the PNO truncation error on the environment shift is even below 1 meV. We thus conclude that a PNO truncation threshold of 10^{-8} is sufficient to ensure a qualitatively correct description of the environment-induced shifts for the investigated TAPPs.

C. Timings and scaling with system size

The computational performance of the implementation was evaluated for compounds (**2**) and (**3**) by determining wall times of conventional supermolecular and FDE calculations for various system sizes with either one or two molecules as the target subsystem for the FDE calculations. The supermolecular calculations were performed with the same mix of basis sets as the FDE calculations together with the RI-J approximation. All computational wall times have been determined for ground state (FDE-)Hartree–Fock calculations followed by a PNO–CIS(D) excitation energy calculation of four excitations on two Intel(R) Xeon(R) Gold 6230 CPUs with 2.10 GHz using OMP parallelization on 40 cores in total with a maximum available memory of 192 Gigabytes. Figure 4 shows the obtained wall times against the number of basis functions of the total system on a logarithmic scale. A breakdown of these timings can be found in the supplementary material.

TABLE III. Excitation energy ω, environment induced shift $\Delta_{\text{env}}\omega$, and the corresponding truncation errors $\Delta_{\text{trunc}}\omega$ and $\Delta_{\text{trunc}}(\Delta_{\text{env}}\omega)$ in eV of the first four excitations computed with the CC2 method of (**2**) within the largest tested cluster.

	ω	ω	$\Delta_{\text{trunc}}\omega$	$\Delta_{\text{env}}\omega$	$\Delta_{\text{env}}\omega$	$\Delta_{\text{trunc}}(\Delta_{\text{env}}\omega)$
Method	CC2	PNO-CC2	PNO-CC2	FDE-CC2	FDE-PNO-CC2	FDE-PNO-CC2
Reference	⋯	⋯	CC2	CC2	PNO-CC2	FDE-CC2
S_1	2.946	2.964	$+18.25 \cdot 10^{-3}$	$+8.52 \cdot 10^{-3}$	$+13.16 \cdot 10^{-3}$	$+4.64 \cdot 10^{-3}$
S_2	3.028	3.057	$+29.71 \cdot 10^{-3}$	$+27.11 \cdot 10^{-3}$	$+25.92 \cdot 10^{-3}$	$-1.19 \cdot 10^{-3}$
S_3	3.142	3.191	$+48.83 \cdot 10^{-3}$	$+169.61 \cdot 10^{-3}$	$+157.51 \cdot 10^{-3}$	$-12.10 \cdot 10^{-3}$
S_4	3.149	3.208	$+59.21 \cdot 10^{-3}$	$+169.80 \cdot 10^{-3}$	$+141.88 \cdot 10^{-3}$	$-27.92 \cdot 10^{-3}$

Published under an exclusive license by AIP Publishing

TABLE IV. Excitation energy ω, environment induced shift $\Delta_{\text{env}}\omega$, and the corresponding truncation errors $\Delta_{\text{trunc}}\omega$ and $\Delta_{\text{trunc}}(\Delta_{\text{env}}\omega)$ in eV of the first four excitations computed with the CC2 method of (**1**) within the largest tested cluster.

	ω	ω	$\Delta_{\text{trunc}}\omega$	$\Delta_{\text{env}}\omega$	$\Delta_{\text{env}}\omega$	$\Delta_{\text{trunc}}(\Delta_{\text{env}}\omega)$
Method	CC2	PNO-CC2	PNO-CC2	FDE-CC2	FDE-PNO-CC2	FDE-PNO-CC2
reference	⋯	⋯	CC2	CC2	PNO-CC2	FDE-CC2
S_1	3.063	3.060	$-2.60 \cdot 10^{-3}$	$+9.58 \cdot 10^{-3}$	$+9.77 \cdot 10^{-3}$	$+0.19 \cdot 10^{-3}$
S_2	3.221	3.235	$+14.47 \cdot 10^{-3}$	$+34.85 \cdot 10^{-3}$	$+26.78 \cdot 10^{-3}$	$-8.07 \cdot 10^{-3}$
S_3	3.229	3.238	$+8.80 \cdot 10^{-3}$	$+148.93 \cdot 10^{-3}$	$+161.31 \cdot 10^{-3}$	$+12.38 \cdot 10^{-3}$
S_4	3.231	3.241	$+9.42 \cdot 10^{-3}$	$+164.36 \cdot 10^{-3}$	$+167.02 \cdot 10^{-3}$	$+2.66 \cdot 10^{-3}$

For compound (**2**), the computation time of the FDE calculations with a monomer as the target subsystem initially increases sublinearly with the number of basis functions N_{bas}, but increases to $k \times N_{bas}^{1.98}$, i.e., quadratically with the overall system size. This behavior arises because for small systems the computation time is dominated by the computation of the target subsystem, including the excitation energies. Additional subsystems in the environment do not lead to a significant increase in computation time. As the size of the total system increases, the integration grid also increases, resulting in higher computational costs for the embedding potential, especially the electrostatic potential. This, along with the linear increase in computation time for the FDE method with the number of subsystems, leads for the current implementation to a quadratic scaling with the number of basis functions above a certain system size. In this case, the point is reached between 8.4 k and 15.2 k basis functions. It should be pointed out that this behavior with respect to the basis functions only occurs because the system size is also increased. An increase in basis functions without any change in system size will lead to a same behavior as in supermolecular calculations. The quadratic scaling with the overall system size can be avoided with fast multipole methods, but this is beyond the scope of the present work.

For the FDE calculations with a TAPP dimer as the target subsystem, only the lower scaling behavior is observed within the range of system sizes used here, but a similar behavior for larger environments as for the FDE calculations with the monomer as target subsystem is expected.

The computation times for the supermolecular calculations exhibit even with the PNO-based implementation a steeper scaling compared to the FDE calculations. Here, the computation time is dominated by the calculation of the excitation energies. From the available data points, we can deduce an approximate power law of $k \times N_{bas}^{2.99}$ for the wall time of these calculations in agreement with the scaling reported in Ref. 35 although the effective scaling varies with the system size, structure, and basis set depending on the onset of integral screening and PNO truncation.

The different scaling of the computation time with the number of basis functions between the FDE method and supermolecular calculations allows for the computation of much larger systems with the FDE approach. This can be shown by the largest system for which

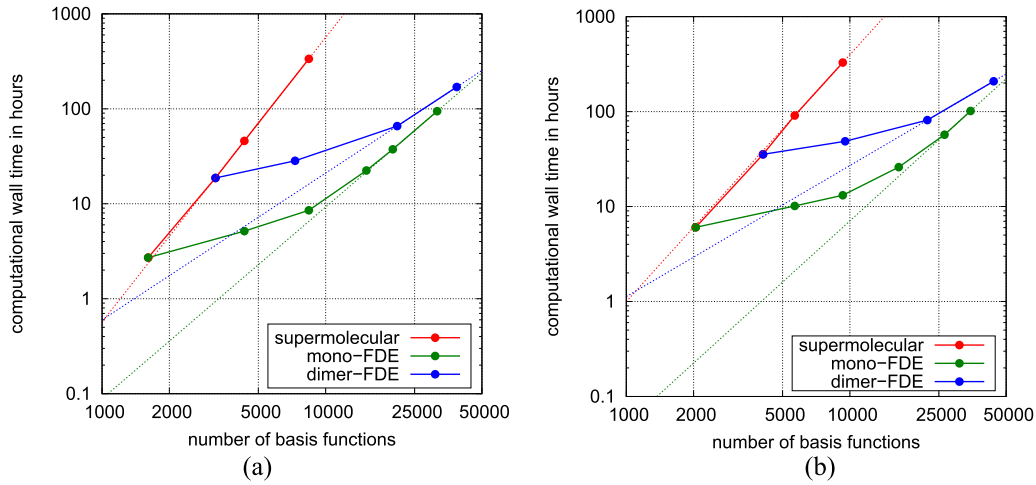


FIG. 4. Computational wall time vs the number of basis function for (**2**) (left) and for (**3**) (right) of various excitation energy calculations with the CIS(D) method. The dashed lines represent the functions $f(N_{bas}) = k \times N_{bas}^{a}$ that were numerically fitted to the last two data points of each method. Further information to the fit can be found in the supplementary material. (a) *bay*-C_2F_5-TAPP-H_4F_4. (b) *all*-C_3F_7-TAPP-Cl_4Br_4.

Published under an exclusive license by AIP Publishing

the wall times were determined for both methods and which consists of 8.4 k basis functions and 528 atoms. For this system, the FDE calculation was 39 times faster than the supermolecular calculation, saving 327 h of wall time.

Compound (**3**) [see Fig. 4(b)] shows a similar behavior for all methods. The wall times of FDE calculations with a monomer as the target subsystem show at the beginning a comparably slow increase in computation time with the number of basis functions and for larger systems an increase with $k \times N_{bas}^{1.82}$. With a dimer as the target subsystem, again only the slow increase within this test series is visible. For the supermolecular calculations, an increase in computation time with the number of basis functions of $k \times N_{bas}^{2.75}$ is observed. This is slightly lower compared to (**2**) probably due to the larger distance between the subsystems, which leads to more negligible pairs in the calculation of the excitation energies. The largest system of compound (**3**) calculated within the supermolecular basis and with the FDE approach consists of 9.3 k basis functions and 486 atoms. For this system, the FDE calculation was 25 times faster than the supermolecular approach and could so save 315 h of wall time.

Compared to the perturbative CIS(D) approach, the iterative methods ADC(2) and CC2 require 10–100 times more CPU time for the calculation of the excitation energies for the active subsystem depending on the convergence threshold for the eigenvalue problem. Since this post-HF step does not affect the computation time for the FaT iterations, the scaling behavior of the computation times is similar with these methods; only the point at which the costs of the FDE step dominate is shifted to larger environments.

D. Convergence of the excitation energies with the environment size

We also investigated how large the environment needs to be for converged results for the excitation energies in the target subsystem. For this purpose, 18 excitation energies were computed for four different radii for three different molecular crystals employing the CIS(D).

Table V shows the lowest ten excitation energies for compound (**2**). For the clusters obtained with radii 10 and 12 Å, the target molecule is not surrounded by neighbor molecules on all sides. First, with 15 Å, the π system of the central molecule is surrounded entirely either by neighbor molecules or $-C_2F_5$ side chains. Up to this point, the excitation energies show variations >10 meV. From the cluster for 15 Å and to that for 20 Å, the excitation energies change at most by about 0.001 eV. We thus conclude that in this case, 20 subsystems for the environment are sufficient to converge the environment-induced shifts. The largest change of 0.113 eV is found for the 9th excitation energy between none and the first four environment subsystems. For the 9th excitation, the difference in excitation energy between the isolated monomer and the monomer surrounded by 44 molecules is the highest with 0.181 eV. The environment-induced shifts are expected to become, in general, larger for higher excitation energies as the orbitals into which the electrons are excited become more diffuse and have a larger overlap with the electron density of neighboring molecules. With a few exceptions, the excitation energies of the TAPPs are all blue shifted with the influence of the environment.

Table VI shows the excitation energies for compound (**3**). Its geometric structure is similar to that of (**2**) only with a slightly larger side chain ($-C_3F_7$ instead of $-C_2F_5$), and we observe a similar convergence of the environment-induced shifts with the cluster size, in particular, only minor changes <10 meV between the clusters obtained with a 15 and 20 Å radius. We thus expect that the excitation energies are converged within 10 meV with the size of the environment. The largest changes are observed between the clusters for 13 and 15 Å, indicating the importance of the additional molecules added in this step to the environment. In contrast to compound (**2**), about half of the excitation energies are red shifted by the interaction with the environment. The origin for the change in this trend from (**2**) to (**3**) is most likely the larger distance between the π systems of neighboring TAPP molecules in the crystal with the larger $-C_3F_7$ side chain. The increased distance reduces the Pauli repulsion between the electrons in the active target subsystem and the environment, which is usually in excited states larger than in the ground states. This is corroborated by the fact that most excitation energies increase between none and four environment subsystems, while the red shifts mostly happen when more distant neighbor molecules

TABLE V. Environment-induced shifts of the first ten excitation energies, computed with the CIS(D) method, in eV of compound (**2**) for different sizes of the environment.

	ω	$\Delta_{env}\omega$			
Radius (Å)	0	10	12	15	20
Env.[a]	0	4	10	20	44
S_1	3.114	+0.013	+0.011	+0.027	+0.027
S_2	3.250	+0.018	+0.019	+0.005	+0.005
S_3	3.697	+0.001	+0.004	−0.027	−0.026
S_4	3.702	+0.041	+0.034	−0.002	−0.002
S_5	3.749	−0.005	−0.001	+0.077	+0.077
S_6	3.898	−0.034	−0.028	−0.029	−0.029
S_7	3.898	+0.023	+0.025	−0.003	−0.003
S_8	4.138	+0.019	+0.020	+0.004	+0.004
S_9	4.307	+0.113	+0.103	+0.182	+0.181
S_{10}	4.638	+0.019	+0.020	−0.001	+0.000

[a]Number of environment subsystems.

TABLE VI. Environment-induced shifts for the first ten excitation energies, computed with the CIS(D) method, in eV of compound (**3**) for different sizes of the environment.

	ω	$\Delta_{env}\omega$			
Radius (Å)	0	10	13	15	20
Env.[a]	0	4	8	16	36
S_1	2.815	+0.005	+0.006	−0.027	−0.026
S_2	2.930	−0.019	−0.019	−0.021	−0.021
S_3	3.115	+0.038	+0.042	−0.019	−0.012
S_4	3.192	+0.029	+0.033	−0.031	−0.027
S_5	3.395	+0.044	+0.045	−0.007	−0.005
S_6	3.452	−0.008	−0.011	+0.044	+0.040
S_7	3.469	+0.024	+0.023	+0.050	+0.047
S_8	3.519	+0.039	+0.042	+0.033	+0.038
S_9	4.000	+0.036	+0.038	−0.054	−0.051
S_{10}	4.021	+0.045	+0.042	+0.055	+0.053

[a]Number of environment subsystems.

Published under an exclusive license by AIP Publishing

are included in the larger clusters. The latter should mainly interact electrostatically with the central molecule. The red shift of excitation energies originate usually from a decrease of the orbital energies for the virtual orbitals by favorable electrostatic interactions with the environment. Only for the second excitation, a decrease of the excitation energies for the small environment is observed. This could be explained by an increase of the orbital energy for the occupied molecular orbital out of which an electron is excited. Again, the largest changes in excitation energies are observed for the higher excitations because electrons are transferred into orbitals, which are more diffuse and, therefore, interact more strongly with the environment.

The excitation energies of (**1**) are shown in Table VII. Here, we used smaller radii for the environment because the molecular crystal is packed much more densely due to the lack of fluorocarbon side chains at the positions labeled with R in Fig. 1. Although the number of molecules around the target subsystem is similar to the other two molecular crystals, the excitation energies still show some variation between the two largest clusters. For example, the fourth excitation energy still changes by −0.045 eV. The highest changes in excitation energy between the systems without environment and 40 surrounding molecules are 0.155 eV for S_4 and 0.120 eV for S_3. The origin of long range interactions in this system could be a larger polarization of the closest neighbors by theirs neighbors because of the smaller intermolecular distances in the crystal for this compound.

E. Embedded TAPP dimer

Finally, we studied the excitation energies for embedded TAPP dimers. Table VIII lists the lowest excitation energies for a dimer of compound (**2**). Here, we see almost no changes between the last two radii and can therefore expect that the excitation energies are converged with respect to the size of the environment. In addition, the changes between the radii of 10 and 15 Å are rather small compared to the changes seen with the monomer as the target subsystem. The largest change in an excitation energy between these radii is seen for S_{10} with −0.027 eV. Most of the changes in the excitation energies already occurs in the step from the isolated dimer to six surrounding subsystems. Further changes are comparatively small. Thus, the largest effect on the dimer system can be achieved with a relatively small environment for this system. The difference in the converged excitation energies of the monomer and the dimer demonstrates the effect of the missing response of the environment in the case of the FDEu approach. Due to electronic coupling beyond the dimer, excitation energies that are directly comparable with experimental results for TAPP crystals could only be obtained with the FDEc method, which is beyond the scope of the current work.

Table IX shows the excitation energies for a dimer of compound (**3**) located in molecular clusters of different size as extracted from the periodic crystal. Between the last two radii, only minor changes up to 0.008 eV in the excitation energies occur. Thus, it can be assumed that the excitation energies are converged with respect to the size of the environment. Compared to the monomer as the target subsystem, the changes in the excitation energies are rather

TABLE VII. Environment-induced shifts for the first ten excitation energies, computed with the CIS(D) method, in eV of compound (**1**) for different sizes of the environment.

	ω	$\Delta_{env}\omega$			
Radius (Å)	0	8	10	12	15
Env.[a]	0	4	10	20	40
S_1	3.240	+0.015	+0.016	+0.028	+0.028
S_2	3.299	+0.050	+0.039	+0.004	+0.001
S_3	3.555	−0.012	+0.020	+0.107	+0.120
S_4	3.585	+0.041	+0.168	+0.200	+0.155
S_5	4.164	+0.054	+0.072	+0.025	+0.016
S_6	4.199	+0.066	+0.069	+0.074	+0.066
S_7	4.276	+0.027	−0.008	+0.005	+0.002
S_8	4.346	−0.003	−0.022	−0.030	+0.015
S_9	4.398	+0.078	−0.040	+0.040	+0.035
S_{10}	4.562	−0.058	−0.034	−0.038	+0.016

[a]Number of environment subsystems.

TABLE VIII. Environment-induced shifts for the first ten excitation energies, computed with the CIS(D) method, in eV of the dimer of compound (**2**) for different sizes of the environment.

	ω	$\Delta_{env}\omega$		
Radius (Å)	0	10	15	20
Env.[a]	0	6	26	52
S_1	2.919	+0.013	+0.010	+0.009
S_2	3.054	−0.059	−0.067	−0.068
S_3	3.115	+0.012	+0.023	+0.025
S_4	3.137	+0.013	+0.023	+0.024
S_5	3.181	+0.015	+0.005	+0.006
S_6	3.265	+0.020	+0.010	+0.010
S_7	3.599	+0.018	+0.011	+0.009
S_8	3.602	+0.076	+0.062	+0.060
S_9	3.673	+0.029	+0.005	+0.007
S_{10}	3.720	−0.004	−0.031	−0.031

[a]Number of environment subsystems.

TABLE IX. Environment-induced shifts for the first ten excitation energies, computed with the CIS(D) method, in eV of the dimer of compound (**3**) for different sizes of the environment.

	ω	$\Delta_{env}\omega$		
Radius (Å)	0	10	15	20
Env.[a]	0	6	20	44
S_1	2.829	+0.004	−0.007	−0.005
S_2	2.876	−0.001	−0.012	−0.010
S_3	2.950	+0.009	−0.016	−0.014
S_4	2.950	+0.007	−0.020	−0.018
S_5	3.147	−0.012	−0.013	−0.013
S_6	3.147	−0.009	−0.012	−0.011
S_7	3.219	+0.010	−0.022	−0.014
S_8	3.220	+0.012	−0.018	−0.010
S_9	3.514	+0.007	−0.043	−0.039
S_{10}	3.517	+0.002	−0.047	−0.043

[a]Number of environment subsystems.

Published under an exclusive license by AIP Publishing

small. It is observed, however, that the 15 Å environment overestimates the induced shifts, which are slightly reduced when increasing the environment cluster.

V. CONCLUSION

Frozen density embedding offers a straightforward, almost black-box way to reduce the costs for the calculation of properties for systems that consist of several only weakly interacting molecules. A large reduction of computational costs can, in particular, be obtained when a system can be divided into small subsystems. Unfortunately, this is not always possible, for example, in the case of complex chromophores, which can lead to large subsystems. This can in turn lead to long computational times when these subsystems are studied, even with second-order correlation methods, e.g., CIS(D), ADC(2), or CC2.

As a solution to this problem, we presented a combination of frozen density embedding with pair natural orbital-based local correlation methods within the pnoccsd program of the TURBOMOLE package. The new extended FDE implementation is applicable for an arbitrary number of subsystems and evaluated the embedding potentials only within the basis of the active subsystem, avoiding the calculation of integrals for the supermolecular basis. It has been implemented at the Hartree-Fock and DFT levels in the dscf and ridft programs. In the latter program, it can be used together with the RI approximation. At the correlated wavefunction level, it has been implemented for MP2, CIS(D), ADC(2), and CC2 in the ricc2 and pnoccsd programs that exploit the resolution-of-the-identity (RI) and the pair natural orbital (PNO) approximations. Excitation energies can be computed within the frozen solvent approximation or the post-SCF reaction field coupling.

We investigated the importance of the post-SCF kernel contributions for excitation energies. The latter originate from the non-linear dependence of the interaction energy on the density of the embedded subsystem. It turned out that they are most of the time small. For the TAPPs that have been used in the current work to study the computational performance of the implementation, test calculations for compound (**2**) demonstrated that the post-SCF kernel contributions are insignificant and can be neglected for TAPPs.

Furthermore, we investigated the effect of the PNO truncation error on environment-induced shifts in the excitation energies of an embedded subsystem. For two TAPP systems, we demonstrate that the truncation error on the environment-induced shifts in valence excitation energies is significantly smaller than the shift themselves and that, thus, the additional approximations made in the PNO-based implementation have only an insignificant effect on the accuracy of the predicted environment-induced shifts.

One aim of the current work was to reduce the computational effort for the calculation of excitation energies in large systems consisting of several weakly interacting molecules. The computational performance for the combination FDE with PNO-based local methods was tested against conventional supermolecular calculations in Sec. IV C. The results demonstrate that large savings can be achieved with this combination. In the case of compound (**2**), the FDE calculation was 39 times faster than the supermolecular calculation for the largest system computed with both methods.

Finally, the behavior of the excitation energy with respect to the size of the embedding environment was investigated for subsystems consisting of either a monomer or a dimer. This showed that the excitation energies converge for the investigated TAPPS with a relatively small number of environment subsystems for an embedded dimer with even less subsystems than for an embedded monomer.

Overall, we demonstrate the capabilities of this combination both in terms of the overall size of the system and in terms of the size of individual subsystems and could show that the accuracy of the environment-induced shift is not significantly affected by the PNO approximation.

SUPPLEMENTARY MATERIAL

See the supplementary material for the computational wall times, the results of the numerical fits, and all excitation energies.

ACKNOWLEDGMENTS

The authors acknowledge TURBOMOLE GmbH for funding. C.H. acknowledges the support from the Deutsche Forschungsgemeinschaft within Priority Program No. SPP 1807 (Grant No. HA 25888/10-1). This work was funded by the Deutsche Forschungsgemeinschaft (DFG, German Research Foundation) under Germany's Excellence Strategy—Grant No. EXC 2022-390677874—RESOLV. S.H. acknowledges support from the Deutsche Forschungsgemeinschaft through SFB 1249 "N-Heteropolycycles as Functional Materials" (Project No. B07).

AUTHOR DECLARATIONS

Conflict of Interest

The authors have no conflicts to disclose.

Author Contributions

Robert S. Treß: Investigation (equal); Writing – original draft (equal). **Jing Liu**: Writing – original draft (supporting). **Christof Hättig**: Writing – review & editing (equal). **Sebastian Höfener**: Writing – review & editing (equal).

DATA AVAILABILITY

The data that support the findings of this study are available within the article and its supplementary material.

REFERENCES

[1] P.-F. Loos, A. Scemama, and D. Jacquemin, J. Phys. Chem. Lett. **11**, 2374 (2020).
[2] S. Miertuš, E. Scrocco, and J. Tomasi, Chem. Phys. **55**, 117 (1981).
[3] A. Klamt and G. Schüürmann, J. Chem. Soc., Perkin Trans. 2 **5**, 799 (1993).
[4] A. V. Marenich, C. J. Cramer, and D. G. Truhlar, J. Phys. Chem. B **113**, 6378 (2009).
[5] A. Warshel and M. Levitt, J. Mol. Biol. **103**, 227 (1976).
[6] E. Brunk and U. Rothlisberger, Chem. Rev. **115**, 6217 (2015).
[7] H. M. Senn and W. Thiel, Angew. Chem., Int. Ed. **48**, 1198 (2009).
[8] J. M. Olsen, K. Aidas, and J. Kongsted, J. Chem. Theory Comput. **6**, 3721 (2010).

Published under an exclusive license by AIP Publishing

[9]T. Schwabe, K. Sneskov, J. M. Haugaard Olsen, J. Kongsted, O. Christiansen, and C. Hättig, J. Chem. Theory Comput. **8**, 3274 (2012).
[10]N. H. List, J. M. H. Olsen, and J. Kongsted, Phys. Chem. Chem. Phys. **18**, 20234 (2016).
[11]A. Marefat Khah, S. Karbalaei Khani, and C. Hättig, J. Chem. Theory Comput. **14**, 4640 (2018).
[12]T. A. Wesołowski and A. Warshel, J. Phys. Chem. **97**, 8050 (1993).
[13]C. R. Jacob and L. Visscher, J. Chem. Phys. **128**, 155102 (2008).
[14]T. A. Wesołowski, Phys. Rev. A **77**, 012504 (2008).
[15]N. Govind, Y. A. Wang, A. J. R. da Silva, and E. A. Carter, Chem. Phys. Lett. **295**, 129 (1998).
[16]N. Govind, Y. A. Wang, and E. A. Carter, J. Chem. Phys. **110**, 7677 (1999).
[17]T. Klüner, N. Govind, Y. A. Wang, and E. A. Carter, Phys. Rev. Lett. **86**, 5954 (2001).
[18]S. Höfener, A. Severo Pereira Gomes, and L. Visscher, J. Chem. Phys. **136**, 044104 (2012).
[19]S. Höfener, A. S. P. Gomes, and L. Visscher, J. Chem. Phys. **139**, 104106 (2013).
[20]T. A. Wesołowski, S. Shedge, and X. Zhou, Chem. Rev. **115**, 5891 (2015).
[21]J. Neugebauer, J. Chem. Phys. **126**, 134116 (2007).
[22]M. E. Casida and T. A. Wesołowski, Int. J. Quantum Chem. **96**, 577 (2004).
[23]F. Neese, F. Wennmohs, and A. Hansen, J. Chem. Phys. **130**, 114108 (2009).
[24]F. Neese, A. Hansen, and D. G. Liakos, J. Chem. Phys. **131**, 064103 (2009).
[25]S. Sæther, T. Kjærgaard, H. Koch, and I.-M. Høyvik, J. Chem. Theory Comput. **13**, 5282 (2017).
[26]I.-M. Høyvik, Mol. Phys. **118**, 1626929 (2020).
[27]R. H. Myhre, A. M. J. Sánches de Merás, and H. Koch, Mol. Phys. **111**, 1109 (2013).
[28]R. H. Myhre, A. M. J. Sánchez de Merás, and H. Koch, J. Chem. Phys. **141**, 224105 (2014).
[29]R. H. Myhre and H. Koch, J. Chem. Phys. **145**, 044111 (2016).
[30]S. Laricchia, E. Fabiano, and F. Della Sala, J. Chem. Phys. **133**, 164111 (2010).
[31]Development version of TURBOMOLE 2020, a development of University of Karlsruhe and Forschungszentrum Karlsruhe GmbH, 1989-2007, TURBOMOLE GmbH, since 2007; available from http://www.turbomole.org; accessed May 13, 2022.
[32]C. Hättig and F. Weigend, J. Chem. Phys. **113**, 5154 (2000).
[33]B. Helmich and C. Hättig, J. Chem. Phys. **135**, 214106 (2011).
[34]B. Helmich and C. Hättig, J. Chem. Phys. **139**, 084114 (2013).
[35]M. S. Frank and C. Hättig, J. Chem. Phys. **148**, 134102 (2018).
[36]G. Senatore and K. R. Subbaswamy, Phys. Rev. B **34**, 5754 (1986).
[37]M. D. Johnson, K. R. Subbaswamy, and G. Senatore, Phys. Rev. B **36**, 9202 (1987).
[38]P. Cortona, Phys. Rev. B **44**, 8454 (1991).
[39]R. S. Treß, C. Hättig, and S. Höfener, J. Chem. Theory Comput. **18**, 1737 (2022).
[40]T. A. Wesolowski and J. Weber, Chem. Phys. Lett. **248**, 71 (1996).
[41]S. Höfener, Int. J. Quantum Chem. **121**, e26351 (2021).
[42]F. J. Olivares del Valle and J. Tomasi, Chem. Phys. **150**, 139 (1991).
[43]M. Caricato, B. Mennucci, J. Tomasi, F. Ingrosso, R. Cammi, S. Corni, and G. Scalmani, J. Chem. Phys. **124**, 124520 (2006).
[44]M. Caricato, J. Chem. Phys. **135**, 074113 (2011).
[45]K. Sneskov, T. Schwabe, J. Kongsted, and O. Christiansen, J. Chem. Phys. **134**, 104108 (2011).
[46]S. Karbalaei Khani, A. Marefat Khah, and C. Hättig, Phys. Chem. Chem. Phys. **20**, 16354 (2018).
[47]O. Christiansen and K. V. Mikkelsen, J. Chem. Phys. **110**, 8348 (1999).
[48]R. Cammi, J. Chem. Phys. **131**, 164104 (2009).
[49]J. Kongsted, A. Osted, K. V. Mikkelsen, and O. Christiansen, J. Chem. Phys. **118**, 1620 (2003).
[50]S. K. Khani, R. Faber, F. Santoro, C. Hättig, and S. Coriani, J. Chem. Theory Comput. **15**, 1242 (2019).
[51]O. Christiansen, H. Koch, and P. Jørgensen, Chem. Phys. Lett. **243**, 409 (1995).
[52]J. Schirmer, Phys. Rev. A **26**, 2395 (1982).
[53]A. B. Trofimov and J. Schirmer, J. Phys. B: At., Mol. Opt. Phys **28**, 2299 (1995).
[54]M. Head-Gordon, M. Oumi, and D. Maurice, Mol. Phys. **96**, 593 (1999).
[55]C. Hättig, Adv. Quantum Chem. **50**, 37 (2005).
[56]M. Head-Gordon, R. J. Rico, M. Oumi, and T. J. Lee, Chem. Phys. Lett. **219**, 21 (1994).
[57]M. Matena, M. Stohr, T. Riehm, J. Bjork, S. Martens, M. S. Dyer, M. Persson, J. Lobo-Checa, K. Muller, M. Enache, H. Wadepohl, J. Zegenhagen, T. A. Jung, and L. H. Gade, CCDC 747374: Experimental crystal structure determination, 2010.
[58]M. Matena, M. Stöhr, T. Riehm, J. Björk, S. Martens, M. S. Dyer, M. Persson, J. Lobo-Checa, K. Müller, M. Enache, H. Wadepohl, J. Zegenhagen, T. A. Jung, and L. H. Gade, Chem. Eur. J **16**, 2079 (2010).
[59]B. A. R. Günther, S. Höfener, R. Eichelmann, U. Zschieschang, H. Wadepohl, H. Klauk, and L. H. Gade, CCDC 1980431: Experimental crystal structure determination, 2020.
[60]B. A. R. Günther, S. Höfener, R. Eichelmann, U. Zschieschang, H. Wadepohl, H. Klauk, and L. H. Gade, Org. Lett. **22**, 2298 (2020).
[61]B. A. R. Günther, S. Höfener, U. Zschieschang, H. Wadepohl, H. Klauk, and L. H. Gade, CCDC 1908781: Experimental crystal structure determination, 2020.
[62]B. A. R. Günther, S. Höfener, U. Zschieschang, H. Wadepohl, H. Klauk, and L. H. Gade, Chem. Eur. J **25**, 14669 (2019).
[63]T. D. Kühne, M. Iannuzzi, M. Del Ben, V. V. Rybkin, P. Seewald, F. Stein, T. Laino, R. Z. Khaliullin, O. Schütt, F. Schiffmann, D. Golze, J. Wilhelm, S. Chulkov, M. H. Bani-Hashemian, V. Weber, U. Borštnik, M. Taillefumier, A. S. Jakobovits, A. Lazzaro, H. Pabst, T. Müller, R. Schade, M. Guidon, S. Andermatt, N. Holmberg, G. K. Schenter, A. Hehn, A. Bussy, F. Belleflamme, G. Tabacchi, A. Glöß, M. Lass, I. Bethune, C. J. Mundy, C. Plessl, M. Watkins, J. VandeVondele, M. Krack, and J. Hutter, J. Chem. Phys. **152**, 194103 (2020).
[64]J. P. Perdew, K. Burke, and M. Ernzerhof, Phys. Rev. Lett. **77**, 3865 (1996).
[65]M. Ernzerhof and G. E. Scuseria, J. Chem. Phys. **110**, 5029 (1999).
[66]J. VandeVondele and J. Hutter, J. Chem. Phys. **127**, 114105 (2007).
[67]M. Krack, Theor. Chem. Acc. **114**, 145 (2005).
[68]S. Grimme, J. Antony, S. Ehrlich, and H. Krieg, J. Chem. Phys. **132**, 154104 (2010).
[69]M. D. Hanwell, D. E. Curtis, D. C. Lonie, T. Vandermeersch, E. Zurek, and G. R. Hutchison, J. Cheminform. **4**, 17 (2012).
[70]W. Humphrey, A. Dalke, and K. Schulten, J. Mol. Grap. **14**, 33 (1996).
[71]J. Liu, "Beyond molecular properties: computational study of TAPP cluster and bulk phase," Ph.D. thesis, Karlsruher Institut für Technologie (KIT) (2022).
[72]A. Marefat Khah, P. Reinholdt, J. M. H. Olsen, J. Kongsted, and C. Hättig, J. Chem. Theory Comput. **16**, 1373 (2020).
[73]F. Weigend and R. Ahlrichs, Phys. Chem. Chem. Phys. **7**, 3297 (2005).
[74]F. Weigend, Phys. Chem. Chem. Phys. **8**, 1057 (2006).
[75]K. Eichkorn, O. Treutler, H. Öhm, M. Häser, and R. Ahlrichs, Chem. Phys. Lett. **242**, 652 (1995).
[76]S. Laricchia, E. Fabiano, L. A. Constantin, and F. Della Sala, J. Chem. Theory Comput. **7**, 2439 (2011).
[77]A. Hellweg, C. Hättig, S. Höfener, and W. Klopper, Theor. Chem. Acc. **117**, 587 (2007).
[78]G. Knizia, J. Chem. Theory Comput. **9**, 4834 (2013).
[79]S. Corni, R. Cammi, B. Mennucci, and J. Tomasi, J. Chem. Phys. **123**, 134512 (2005).
[80]R. A. Kendall, T. H. Dunning, and R. J. Harrison, J. Chem. Phys. **96**, 6796 (1992).
[81]T. H. Dunning, J. Chem. Phys. **90**, 1007 (1989).
[82]A. Lembarki and H. Chermette, Phys. Rev. A **50**, 5328 (1994).

Published under an exclusive license by AIP Publishing